

---

# Multiple-FM Smoothing by Spectral Dispersion—An Augmented Laser Speckle Smoothing Scheme

## Introduction

Polar-drive (PD)<sup>1–4</sup> implosions on the National Ignition Facility (NIF) require smoothing of the laser-imposed nonuniformities. The spot shape on target is controlled by employing distributed phase plates (DPP's).<sup>5,6</sup> Smoothing by spectral dispersion (SSD)<sup>7–9</sup> smoothes the far-field speckle pattern in a time-integrated sense by continuously changing the near-field phase front of the laser beam. The current configuration of the NIF has SSD in only one dimension (i.e., 1-D SSD), which is insufficient for directly driven targets. A two-dimensional (2-D) SSD system with a 1-THz ultraviolet bandwidth and two color cycles proposed for the NIF provides the requisite smoothing but it is an expensive option that adds considerable complexity.<sup>10</sup> An idea originally suggested by Rothenberg<sup>11</sup> further improved beam smoothing of all spatial frequencies by augmenting the 2-D SSD system with multiple-FM modulators in both dimensions at the expense of both increased complexity and cost. An alternative laser speckle smoothing scheme proposed here employs multiple-FM modulators in a single dimension (MultiFM 1-D SSD) with minimal cost increase and added system complexity since the added modulation can be applied in the all-fiber-optic front-end system. In addition, this system concentrates beam-smoothing improvements on the lower end of the spatial frequencies that most limit direct-drive implosions with a low in-flight aspect ratio.

MultiFM 1-D SSD employs multiple color cycles to improve the smoothing of lower-spatial-frequency nonuniformities without producing resonances at higher spatial frequencies because multiple modulators interact and effectively average the resonant features with a judicious choice of modulator frequencies. MultiFM 1-D SSD attains similar or even faster smoothing rates compared to the full 2-D SSD system, albeit with shorter asymptotic times. Two-dimensional hydrodynamic simulations using *DRACO*<sup>12</sup> show that MultiFM 1-D SSD is sufficient for the targets and pulse shapes analyzed thus far, even for smaller overall bandwidth (in the 0.5-THz range), which means that a single frequency-conversion crystal system can be used for the NIF with significant cost and complexity savings.

## MultiFM Coherence Time

When SSD is employed, smoothing for any spatial frequency can be characterized by an inverse coherence time (or smoothing rate) and an asymptotic nonuniformity. The rms average of the inverse coherence times over all spatial frequencies is equivalent to the effective bandwidth applied to the laser beam; however, this bandwidth is not uniformly distributed over the spatial frequencies imposed in the far-field plane, which range from zero to the highest spatial frequency determined by the diffraction limited spot. The SSD system does not continue to smooth forever but is limited to the characteristic asymptotic level that is determined by the angular divergence of the near field imposed by SSD. Both of these characteristics can be represented by a fitted functional form

$$\sigma^2(t, \ell) = \sigma_0^2(\ell) \frac{t_c(\ell)}{t + t_c(\ell)} + \sigma_{\text{asym}}^2(\ell), \quad (1)$$

where  $\sigma_0^2(\ell) \equiv \sigma^2(0, \ell)$  is the initial value of the nonuniformity and  $\sigma_{\text{asym}}^2(\ell) \equiv \sigma^2(\infty, \ell)$  is the asymptotic level of the nonuniformity for the spatial mode given by  $\ell$ .

After a few coherence times and prior to reaching the asymptotic level, Eq. (1) can be approximated by

$$\sigma^2(t, \ell) \approx \sigma_0^2(\ell) \frac{t_c(\ell)}{t}, \quad t_c < t < t_{\text{asym}}. \quad (2)$$

During this time, the coherence time proportionally affects the level of nonuniformity, whereas the “slope” is given by  $t^{-1}$ . If the coherence time can be decreased by modifying the SSD design, the nonuniformity for a given mode will decrease proportionally. The asymptotic nonuniformity level  $\sigma_{\text{asym}}$  is determined by the angular divergence of the SSD system because this determines the number of independent modes in the far field. Increasing the angular divergence reduces  $\sigma_{\text{asym}}$ .

The smoothing performance of any SSD system, including MultiFM, is accurately calculated using a specialized, time-dependent far-field simulation, like *Waasikwa'*.<sup>13</sup> Figure 114.22 shows the smoothing performance of the  $\ell$ -mode range  $30 < \ell < 60$  for the NIF 1-D SSD system with 10.8 Å of applied IR bandwidth yielding 878 GHz of ultraviolet bandwidth.<sup>(a)</sup> The figure also indicates the relative improvements that could be made for this  $\ell$ -mode range by increasing the applied bandwidth  $\Delta\lambda$  or the angular divergence  $\Delta\theta_{SSD}$ . For  $\ell$  modes lower than the first local maximum in the distributed inverse coherence time (roughly  $\ell < 100$  for systems in this article; see Fig. 114.25), the inverse coherence time is approximately given by  $t_c^{-1} \propto \ell \Delta\lambda N_{cc}$ , where  $N_{cc}$  is the effective number of color cycles. The angular divergence of one dimension is given approximately by  $\Delta\theta_{SSD} \propto \Delta\lambda N_{cc} / \nu_m$ , where  $\nu_m$  is the modulator frequency.

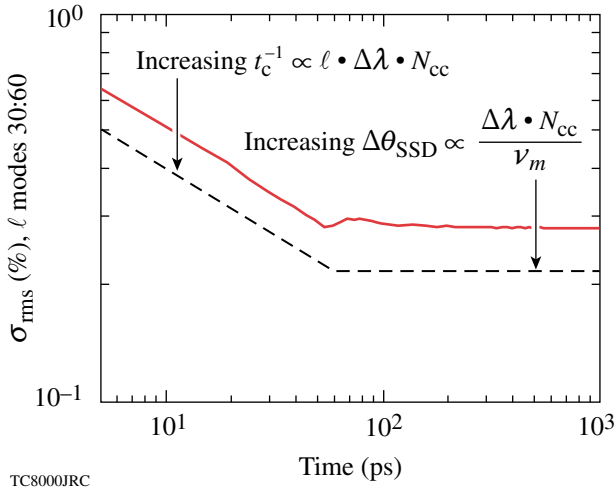


Figure 114.22 Time evolution of the nonuniformity summed over the  $\ell$ -mode range  $30 < \ell < 60$  for the NIF 1-D SSD system with 10.8 Å of applied bandwidth (878-GHz UV). The solid line represents the result of a *Waasikwa'* far-field simulation. The dashed line indicates the improvements possible by altering the coherence time and/or the angular divergence: (1) decreasing the coherence time of a mode proportionally decreases the level of nonuniformity during  $t_c < t < t_{asym}$  and (2) increasing the angular divergence will decrease the asymptotic level  $\sigma_{asym}$ .

Figure 114.23 shows the smoothing effect on the lower  $\ell$  modes by increasing the number of color cycles while holding the bandwidth and angular divergence constant. For early times in the laser pulse (not shown), the initial nonuniformity is the same [ $\sigma^2(t, \ell) \rightarrow \sigma_0^2(\ell)$  as  $t \rightarrow 0$ ] for each case. However,

increasing the number of color cycles delivers asymptotic smoothing performance at earlier times. This illustrates that as the inverse coherence time is increased for this  $\ell$ -mode range, the far field can be smoothed faster and the asymptotic level can be reached earlier.

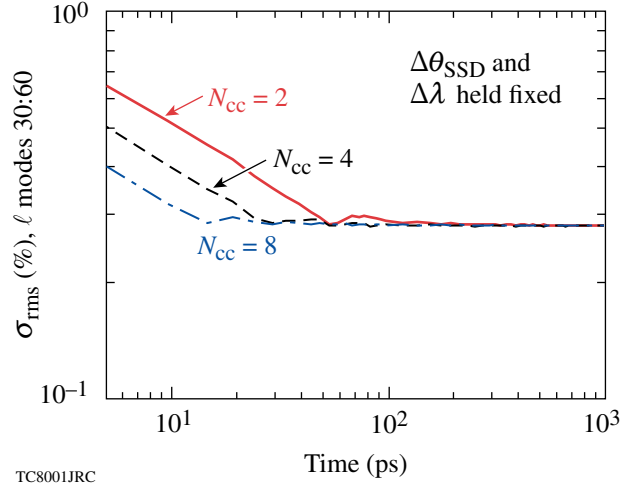


Figure 114.23 Time evolution of the nonuniformity rss-summed over the  $\ell$ -mode range  $30 < \ell < 60$  for three different realizations of a 1-D SSD system. The applied bandwidth and angular divergence are held fixed at 10.8 Å and 100  $\mu$ rad, respectively, while the number of color cycles is varied as 2, 4, and 8, which correspond to modulator frequencies of 17.5, 35.5, and 70.5 GHz, respectively. All three traces represent full *Waasikwa'* far-field simulations. The effective bandwidth is 1.1 THz.

As previously noted, the inverse coherence time is not constant over the entire  $\ell$ -mode range of the far-field intensity pattern. The inverse coherence time for each  $\ell$  mode and the values of  $\sigma_0^2(\ell)$  and  $\sigma_{asym}^2(\ell)$  can be calculated by fitting Eq. (1) to time-dependent *Waasikwa'* far-field simulations, but this is a computationally intensive process. A simplified phenomenological formulation is desirable for evaluating or designing many SSD system variations. However, it is essential that the simple mathematical model given here is verified against a full far-field simulation prior to performing the even-lengthier hydrodynamic simulation. This is done by verifying a final MultiFM system design using the simple  $t_c^{-1}$  model against a time-dependent *Waasikwa'* simulation fitted to Eq. (1).

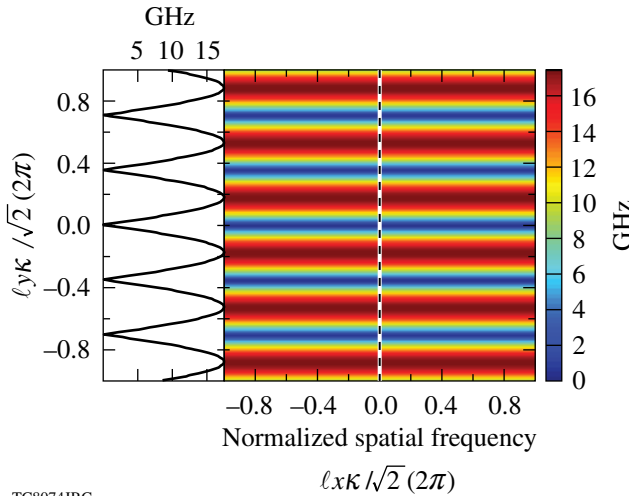
For a 1-D SSD system the inverse coherence time along a single spatial dimension<sup>11</sup> is given by

<sup>(a)</sup>Conventionally, the applied laser bandwidth is specified in two different units to distinguish to which end of the frequency-converted laser system the bandwidth refers. When the bandwidth is given in angstroms (Å), it refers to the bandwidth in the front-end IR system and when the bandwidth is specified in GHz or THz, it refers to the bandwidth following the frequency-conversion crystals in the UV range. An IR bandwidth of 12.3 Å corresponds to 1.0 THz in the UV.

$$t_c^{-1}(\ell_x) = 2\Delta\lambda \sin\left(\frac{1}{2}\ell_x \kappa N_{cc,x}\right) \quad (3)$$

along one of the two spatial-frequency directions, where  $\ell_x \equiv k_{x_{\text{ff}}} r_{\text{tar}}$ ,  $\kappa \equiv f_{\text{NIF}} \lambda_{\text{UV}} / (r_{\text{tar}} D_{\text{NIF}})$ , and  $k_{x_{\text{ff}}}$ ,  $f_{\text{NIF}}$ ,  $\lambda_{\text{UV}}$ ,  $r_{\text{tar}}$ , and  $D_{\text{NIF}}$  are the NIF spatial frequency, focal length, laser wavelength, target radius and near-field diameter, respectively. A similar functional form represents the second dimension for a 2-D SSD system; if no second dimension is included, then  $t_c^{-1}_y = 0$ . For a single-modulator 1-D SSD system, a 2-D plot of the inverse coherence time is shown in Fig. 114.24 for the two-color-cycle, 10.8 Å, 1-D SSD system described in Fig. 114.23. Note that in Fig. 114.24 the inverse coherence time periodically goes to zero for spatial frequencies where no beam smoothing is achieved. Equation (3) defines the inverse coherence time in only a single spatial-frequency dimension, but an azimuthal average is standard practice for comparing the effectiveness of different SSD systems (including MultiFM and 2-D SSD). The inverse coherence time for an effective  $\ell$  mode in the 2-D plane is defined as

$$t_c^{-1}_{\text{rss}}(\ell) \equiv \sqrt{(t_c^{-1}_x)^2 + (t_c^{-1}_y)^2}, \quad (4)$$



TC8074JRC

Figure 114.24

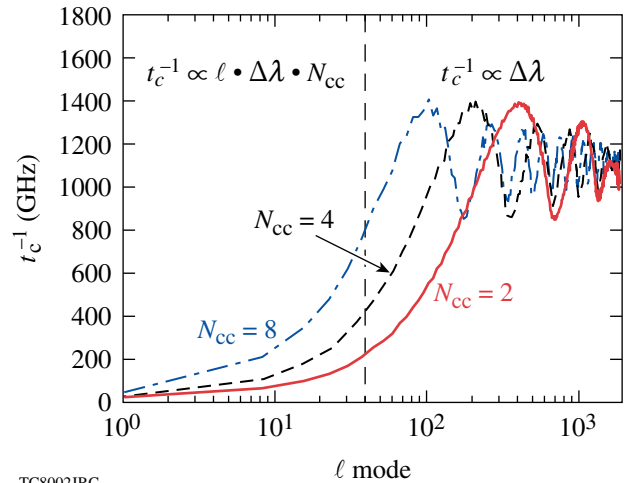
The inverse coherence time  $t_c^{-1}$  (in GHz) plotted in two dimensions as a function of the normalized-spatial-frequency, two-color-cycle system in Fig. 114.23 (1.1 THz, 100  $\mu\text{rad}$ ). Note that the number of zeros counted along the positive or negative axis for non-zero frequencies up to the effective round-aperture cut-off frequency yields the number of color cycles. In this case, there are two zeros along the positive or negative vertical axis. The axis has been normalized to a square NIF aperture and therefore is lengthened by  $\sqrt{2}$  relative to a round aperture. A lineout in the SSD dispersion direction illustrates how the inverse coherence time periodically goes to zero. No beam smoothing is experienced at these spatial frequencies.

where  $\ell \equiv \ell(\theta) = \sqrt{\ell_x^2 + \ell_y^2}$  is the radial  $\ell$  mode. In addition, it is necessary to account for the effect of the near-field beam envelope on the resultant inverse coherence time because the envelope affects the relevant weighting of the contribution of each spatial frequency in the 2-D spatial-frequency plane. The mathematical model of a 1-D or 2-D SSD system is then given by

$$t_c^{-1}(\ell) = \frac{\oint t_c^{-1}_{\text{rss}}(\ell) \text{PSD}_0(\ell) \ell d\theta}{\oint \text{PSD}_0(\ell) \ell d\theta}, \quad (5)$$

where  $\text{PSD}_0(\ell)$  is the spatial-frequency power spectrum of the diffraction-limited spot or single speckle pattern.<sup>16,17</sup> Note that the  $\text{PSD}_0(\ell)$  can be used to analyze the effect of partially filled near-field apertures.

Equation (5) is employed to calculate the inverse coherence time versus  $\ell$  mode for the three realizations of the 1-D SSD system, as shown in Fig. 114.25. These curves illustrate distinct behavior for the large  $\ell$ -mode and low  $\ell$ -mode regions. The mean value of the inverse coherence time yields a measure of the effective bandwidth. For the 1-D SSD systems the



TC8002JRC

Figure 114.25

The inverse coherence time  $t_c^{-1}$  (in GHz) plotted as a function of the spatial  $\ell$ -mode number for the three different 1-D SSD systems described in Fig. 114.23. The number of color cycles is varied as 2, 4, and 8. The divergences are fixed at 100  $\mu\text{rad}$ . Note that the average inverse coherence time for the large  $\ell$  modes is approximately 1.25 $\times$  the applied bandwidth of 878 GHz and that the inverse coherence time for the lower  $\ell$  modes ( $\ell <$  first local maximum) is given by  $t_c^{-1} \propto \ell \Delta\lambda N_{cc}$ . The resultant effective bandwidth is 1.1 THz. The vertical dashed line indicates the approximate distinction between low  $\ell$  and high  $\ell$  modes.

effective bandwidth is 1.1 THz, which is roughly  $1.25\times$  the applied bandwidth for a single modulator system. In the large  $\ell$ -mode range, the inverse coherence time is given roughly by the effective bandwidth. The peak of the first local maximum is  $1.1\sqrt{2}$  of the applied bandwidth, as related to the maximum of Eq. (3) that is azimuthally averaged around the 2-D plane. In the  $\ell$ -mode range lower than the first local maximum, the inverse coherence time is given by

$$t_c^{-1}(\ell) = \Delta\lambda\ell\kappa N_{cc}, \quad (6)$$

which can be understood by taking the small angle approximation to Eq. (3).

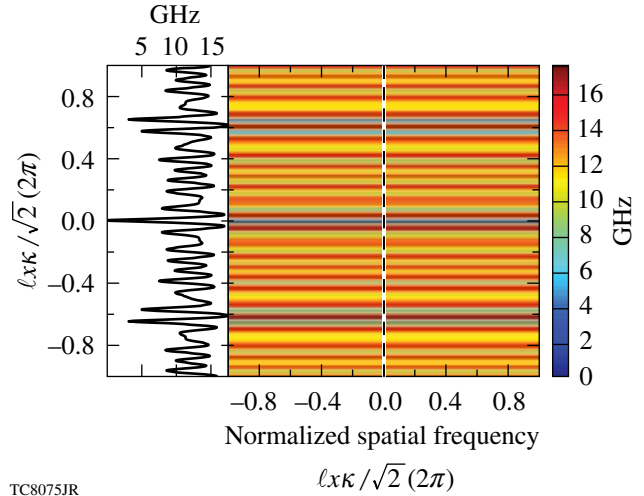
Another feature in Fig. 114.25 is the series of strong resonances in the large  $\ell$ -mode range. This is due to the coherent effect of having multiple color cycles across the near-field plane. Each color cycle is a copy of its neighbors and does not lend to smoothing at the corresponding spatial frequency, which leads to the zeroes of Eq. (3). The zeroes of the resonant features are a 1-D effect, and their relative effect is lessened due to the azimuthal averaging of Eq. (5); however, the zeroes are still present in the 2-D plane and represent spatial frequencies that experience no smoothing and are a potential threat in an ICF implosion due to hydrodynamic instabilities. The only smoothing that these modes get is from multiple beam overlap on target.

The resonant features caused by multiple color cycles can be mitigated with MultiFM if the modulator frequencies are judiciously chosen. The effect of multiple overlaid patterns dramatically reduces the range of spatial frequencies that do not benefit from beam smoothing, as illustrated in Fig. 114.26. In the near field, the application of MultiFM in 1-D takes the form

$$E(x, y) = E_0(x, y) \prod_{n=1}^N e^{i3\delta_n \sin[\omega_n(t + \xi_x x)]}, \quad (7)$$

where  $E_0(x, y)$  is the near-field beam envelope and  $\delta_n$ ,  $\omega_n$ , and  $\xi_x$  are modulation depth, frequency, and grating dispersion for the  $n$ th modulators, respectively.

To calculate the inverse coherence time for the MultiFM case, Eq. (3) can be generalized by root-sum-square (rss) summing the values for each modulator. This approximation is valid when the modulation frequencies are incommensurate and the mixing of the modes in the far field temporally integrates to zero since terms like  $\cos(\omega_m t) \cdot \cos(\omega_n t)$  average to zero



TC8075JR

Figure 114.26

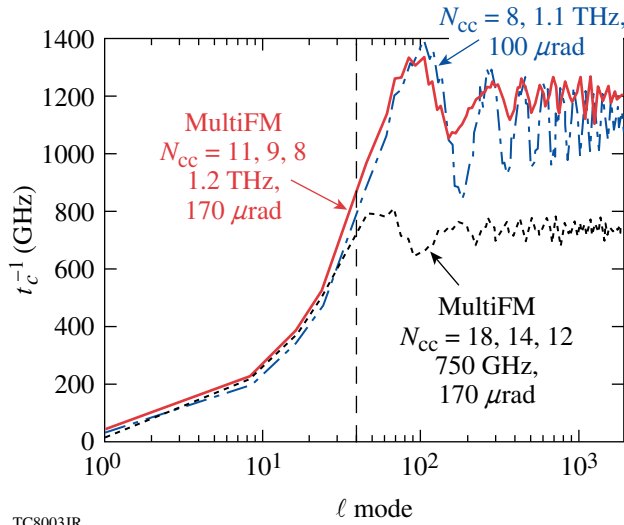
The inverse coherence time  $t_c^{-1}$  (in GHz) plotted in two dimensions as a function of normalized spatial frequency for a MultiFM 1-D SSD system employing three modulators at frequencies of 65, 75, and 95 GHz ( $N_{cc} = 8, 9, \text{ and } 11$ , respectively) with a combined divergence of  $175 \mu\text{rad}$  and effective ultraviolet bandwidth of 1.2 THz. A lineout in the 1-D SSD dispersion direction illustrates the significant improvement in beam smoothing compared to Fig. 114.24. Note that the inverse coherence time goes to zero for all modulators at the origin by definition.

when  $m$  is not equal to  $n$ . A three-modulator MultiFM case is compared in Fig. 114.27 to a single-modulator, eight-color-cycle case. Three modulators at frequencies of 65, 75, and 95 GHz ( $N_{cc} = 8, 9, \text{ and } 11$ , respectively) produce a combined divergence of  $175 \mu\text{rad}$  and effective ultraviolet bandwidth of 1.2 THz. Beam-smoothing rates are comparable for low  $\ell$  modes, but the MultiFM configuration outperforms the single modulator for high  $\ell$  modes due to the overlapped effect of multiple modulators, each with multiple color cycles. The effective color-cycle number is weighted by the bandwidth of each modulator,

$$N_{cc_{mFM}} \simeq \frac{\sqrt{\sum_{n=1}^N (N_{cc_n} \Delta\lambda_n)^2}}{\sqrt{\sum_{n=1}^N \Delta\lambda_n^2}}, \quad (8)$$

while the effective bandwidth and angular divergence can be estimated by rss-summing the contributions from each modulator. The total angular divergence, however, can have significant energy in the wings of the distribution as far out as the linear sum of the individual divergences.

An important observation is that improved lower  $\ell$ -mode performance can also be achieved while decreasing the total

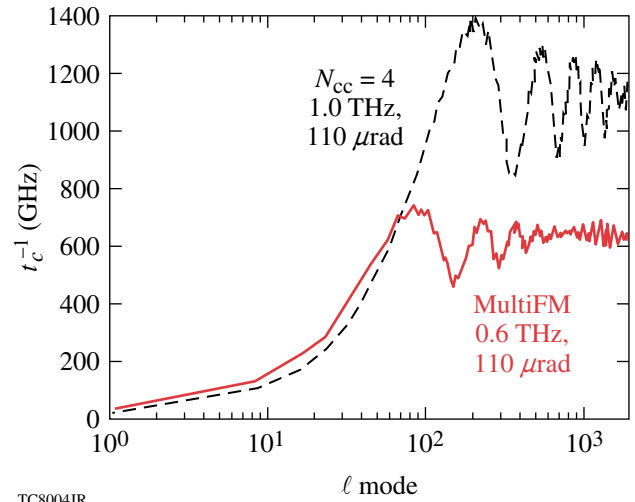


TC8003JR

Figure 114.27

Azimuthally averaged inverse coherence time plotted as a function of spatial  $\ell$ -mode number for an eight-color-cycle, 1-D SSD system (eight color cycles, 1.1 THz, 100  $\mu\text{rad}$ ) and MultiFM 1-D SSD system (8, 9, and 11 color cycles, 1.2 THz, 170  $\mu\text{rad}$ ). Another MultiFM 1-D SSD realization is also shown (12, 14, and 18 color cycles, 750 GHz, 170  $\mu\text{rad}$ ) using three modulators at 68, 77, and 94 GHz, respectively, but a smaller effective bandwidth of 750 GHz. The vertical dashed line indicates the approximate distinction between low  $\ell$  and high  $\ell$  modes.

applied bandwidth, as long as the product  $\Delta\lambda \cdot N_{cc}$  and the angular divergence  $\Delta\theta$  are held constant. In general, high  $\ell$ -mode nonuniformities decouple much sooner from directly driven targets with low in-flight aspect ratios than lower  $\ell$  modes, which implies that the larger  $\ell$  modes do not utilize all the potential smoothing of these modes. MultiFM 1-D SSD makes it possible to reduce the total bandwidth applied while maintaining the same performance of the lower  $\ell$  modes. This phenomenon is depicted in the third plot (dashed) in Fig. 114.27, where a different set of modulation frequencies and color cycles achieves the same performance with a lower effective bandwidth of 750 GHz. Likewise, the two-modulator MultiFM 1-D SSD system shown in Fig. 114.28 matches the low  $\ell$ -mode performance with only 600-GHz effective bandwidth and 110  $\mu\text{rad}$  of divergence. Two-dimensional hydrodynamic DRACO simulations of NIF direct-drive targets with 1- $\mu\text{m}$  (rms) inner ice roughness, 30-ps (rms) mistiming, 50- $\mu\text{m}$  (rms) beam mispointing, and 8% (rms) energy imbalance for a 1.5-MJ CH-foam target in a symmetric-drive configuration show that this MultiFM system provides sufficient beam smoothing to achieve ignition. Further research is underway to determine if the bandwidth and the total energy delivered to target can be reduced, as well as to investigate MultiFM 1-D SSD for polar-drive implosions. Significant costs and complexity could be avoided on the NIF



TC8004JR

Figure 114.28

The inverse coherence time plotted as a function of spatial  $\ell$  mode number for a four-color-cycle, 1-D SSD system and a low  $\ell$ -mode-matching MultiFM 1-D SSD system with two modulators and lower applied bandwidth. This realization of a MultiFM 1-D SSD system employs two modulators at frequencies of 55 and 60 GHz ( $N_{cc} = 9$  and 10, respectively) and used a combined divergence of 110  $\mu\text{rad}$  and only 600 GHz of effective UV bandwidth.

if the applied bandwidth can be reduced to 0.5 THz, since only a single frequency-tripling crystal would be required.

### MultiFM Divergence

The asymptotic level of nonuniformity,  $\sigma_{\text{asym}}$ , of the lower  $\ell$  modes is governed by the angular divergence because more-independent speckle modes are created. The angular divergence is ultimately limited by the smallest pinhole in the laser system. The primary concern is pinhole closure during the main drive pulse. Currently, the angular divergence  $\Delta\theta_{\text{SSD}}$  for the NIF is limited to 100  $\mu\text{rad}$  (full angle), which is set by a minimum pinhole size of 300  $\mu\text{rad}$ . Dynamic bandwidth reduction<sup>14</sup> should allow the angular divergence to be increased without the risk of pinhole closure since simulations indicate that strong beam smoothing is required only during the initial low-power portion of the laser pulse when significant laser imprinting occurs.<sup>15</sup> The angular divergence of SSD for a single modulator is given by

$$\Delta\theta_{\text{SSD}} \propto \frac{N_{cc}\Delta\lambda}{\nu_m}, \quad (9)$$

where  $\nu_m$  is the modulator frequency. The angular divergence can be increased by increasing the  $N_{cc}\Delta\lambda$  product and/or decreasing the modulator frequency  $\nu_m$ . Current investigations of MultiFM have limited divergence to a maximum full angle of 170  $\mu\text{rad}$ , but increasing this limit could further improve

smoothing of these important modes. Detailed laser imprint experiments will be performed on OMEGA EP with a prototypical NIF beam-smoothing system to establish practical dynamic bandwidth reduction schemes. Additional experiments will also be performed to establish any lower limit of beam smoothing required late in the drive pulse to mitigate adverse laser-plasma interactions.

The asymptotic nonuniformity level and the time it takes to reach this level can be accurately calculated for a square pulse shape due to MultiFM 1-D SSD.<sup>18</sup> The nonuniformity as a function of time can also be calculated for arbitrary pulse shapes and 2-D SSD system configuration but is beyond the scope of this article and will be discussed in a forthcoming article. The asymptotic nonuniformity due to a MultiFM 1-D SSD system is given by

$$\sigma_{\text{asym}}(\ell) = \frac{1}{2\pi} \oint \prod_{n=1}^N J_0[\zeta_n(\ell, \theta)] d\theta, \quad (10a)$$

where

$$\zeta_n(\ell, \theta) \equiv 6\xi_n \sin\left[\pi N_{\text{cc}_n} \frac{\ell}{\ell_c} \cos(\theta)\right], \quad (10b)$$

$J_0$  is a zeroth-order Bessel function of the first kind, and  $\ell_c \equiv 2\pi r_{\text{tar}} D_{\text{NIF}} / (f_{\text{NIF}} \lambda_{\text{UV}})$  is the  $\ell$ -mode cutoff. The angle  $\theta$  is necessary because although the proposed MultiFM beam smoothing is applied only in a single direction, the spectrum is inherently 2-D and it facilitates the azimuthal average. The number of independent states is found by  $N_{\text{states}} = 1 / \sigma_{\text{asym}}^2(\ell)$ . If the coherence time is known for the  $\ell$  mode, then the asymptotic time is given by  $t_{\text{asym}} = t_c N_{\text{states}}$ . The formulation represented in Eqs. (10) is appropriate for all  $\ell$  modes.

The statement that increasing the angular divergence, given by Eq. (9), decreases the  $\sigma_{\text{asym}}$ , given by Eqs. (10), can be understood by examining the arguments of the Bessel function. This applies only to the lower  $\ell$  modes due to the sine function as an argument to the Bessel function and to the multi-color-cycle effects. As the argument of the Bessel function increases, the peak envelope of the Bessel function decreases. For  $\ell$  modes lower than the peak of the first maximum of the sine function, the argument of the Bessel function increases when the product  $\delta_m N_{\text{cc}}$  increases. The product relates to the total angular divergence because  $\delta_m N_{\text{cc}} \propto \Delta \lambda N_{\text{cc}} / (2\nu_m) \propto \Delta \theta$ .

Beam-smoothing performance depends not only on the inverse coherence time and the total divergence but also on the shape of the spectral divergence. Some combinations of modulators yield excellent smoothing rates (inverse coherence time) for a given total divergence, but do not provide adequate beam smoothing due to the spectral distribution. The effectiveness of spectral modes is weighted by their amplitudes. The shape of the spectrum is found by taking the 2-D Fourier transform of the near-field beam with its associated SSD phase front applied but without a phase plate. In general, the shape of the far-field spectrum differs from the shape of the temporal frequency spectrum due to the near-field beam shape. Ideally, modes are evenly weighted for best smoothing performance, but edge-peaked spectra perform better than center-peaked spectra. An example is shown in Fig. 114.29, where the applied bandwidth and total divergences are identical for the two different MultiFM cases. The configuration with a more-uniform divergence but some edge peaking [Fig. 114.29(a)] gives better far-field simulation performance early in time than the strong, center-peaked divergence shown in Fig. 114.29(b), which is illustrated in Fig. 114.29(c).

## Conclusion

Implementing MultiFM 1-D SSD beam smoothing on the NIF is a promising approach to meet the smoothing requirements for polar-drive implosions. It provides the flexibility to tailor the inverse coherence time spectrum to meet the target hydrodynamic-instability requirements while potentially reducing the overall bandwidth of the SSD system. Multiple color cycles are used to increase the performance of the lower  $\ell$  modes and multiple modulators are used to reduce the resonant effects of multiple color cycles. Figure 114.30 shows how the MultiFM 1-D SSD system with 600-GHz effective bandwidth and 110  $\mu\text{rad}$  of divergence described in Fig. 114.28 nearly attains the same target performance for a 1.5-MJ CH-foam target as the baseline 1-THz, 2-D SSD. Future work will extend these results to a 500-GHz MultiFM 1-D SSD system and a 1.0-MJ CH-foam target. It may require increasing the angular divergence and invoking dynamic bandwidth reduction.

## ACKNOWLEDGMENT

This work was supported by the U.S. Department of Energy Office of Inertial Confinement Fusion under Cooperative Agreement No. DE-FC52-08NA28302, the University of Rochester, and the New York State Energy Research and Development Authority. The support of DOE does not constitute an endorsement by DOE of the views expressed in this article.

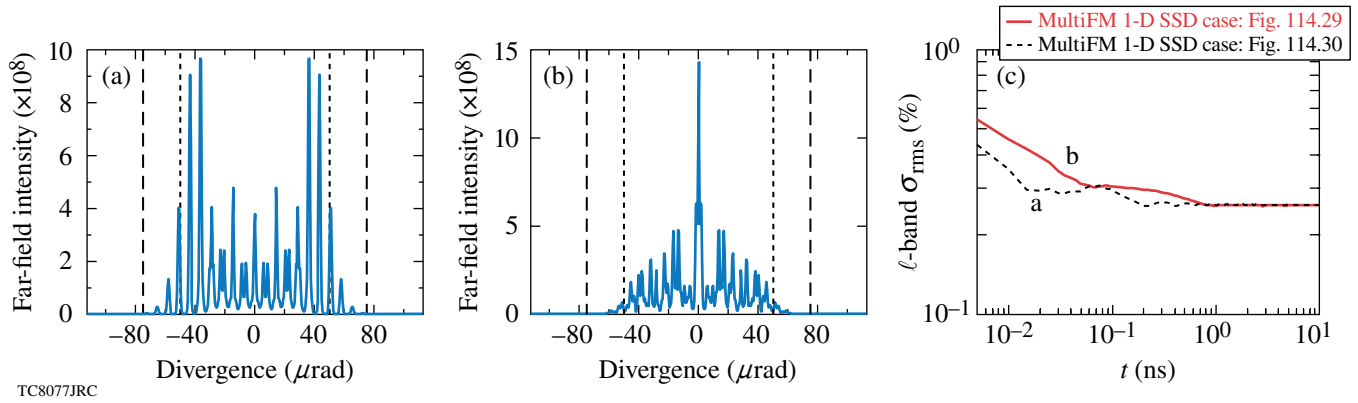


Figure 114.29

Angular divergence, plotted in the far field or pinhole plane, for two different MultiFM 1-D SSD systems with 820-GHz effective bandwidth and 110  $\mu\text{rad}$  of divergence. The modulator frequencies were (a) 61 and 55 GHz with eight and seven color cycles, respectively, and (b) 61 and 45 GHz with eight and five color cycles, respectively. The thin dashed vertical line represents the 100- $\mu\text{rad}$  specification and the thick dashed line represents the 150- $\mu\text{rad}$  boundary. Note how the spectrum in (b) is more widely distributed and edge peaked relative to (a). (c) The nonuniformity calculated by *Waaasikwa*' is rss-summed over  $\ell$  modes 30 to 60 and is plotted as a function of time. Both systems have the same resulting asymptotic value but the system with the edge-peaked spectrum has improved performance early in time.

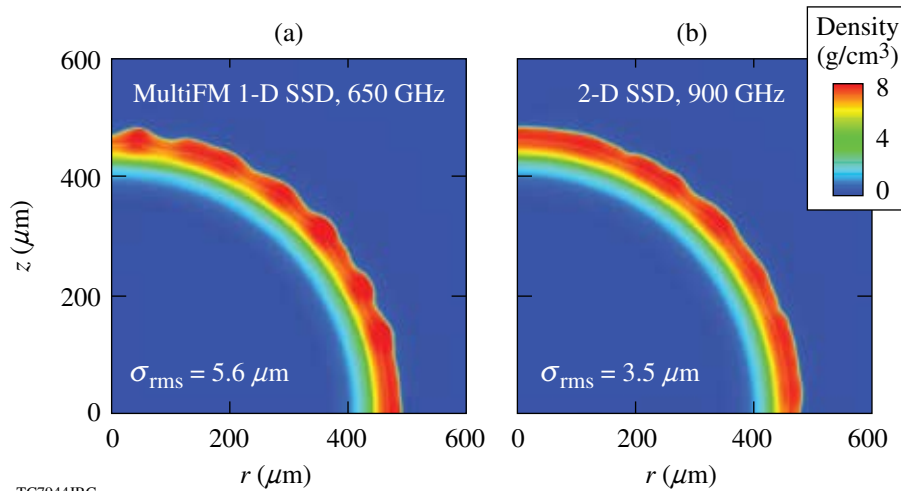


Figure 114.30

1.5-MJ CH-foam target at the end of the acceleration phase for three different SSD systems. (a) MultiFM 1-D SSD described in Fig. 114.28 and (b) 2-D SSD. Both the MultiFM 1-D SSD system and the 2-D SSD system attain nearly 1-D gain.

REFERENCES

1. S. Skupsky, J. A. Marozas, R. S. Craxton, R. Betti, T. J. B. Collins, J. A. Delettrez, V. N. Goncharov, P. W. McKenty, P. B. Radha, T. R. Boehly, J. P. Knauer, F. J. Marshall, D. R. Harding, J. D. Kilkenny, D. D. Meyerhofer, T. C. Sangster, and R. L. McCrory, *Phys. Plasmas* **11**, 2763 (2004).
2. J. A. Marozas, F. J. Marshall, R. S. Craxton, I. V. Igumenshchev, S. Skupsky, M. J. Bonino, T. J. B. Collins, R. Epstein, V. Yu. Glebov, D. Jacobs-Perkins, J. P. Knauer, R. L. McCrory, P. W. McKenty, D. D. Meyerhofer, S. G. Noyes, P. B. Radha, T. C. Sangster, W. Seka, and V. A. Smalyuk, *Phys. Plasmas* **13**, 056311 (2006).
3. R. S. Craxton and D. W. Jacobs-Perkins, *Phys. Rev. Lett.* **94**, 095002 (2005).
4. R. S. Craxton, F. J. Marshall, M. J. Bonino, R. Epstein, P. W. McKenty, S. Skupsky, J. A. Delettrez, I. V. Igumenshchev, D. W. Jacobs-Perkins, J. P. Knauer, J. A. Marozas, P. B. Radha, and W. Seka, *Phys. Plasmas* **12**, 056304 (2005).
5. J. A. Marozas, *J. Opt. Soc. Am. A* **24**, 74 (2007).
6. T. R. Boehly, D. L. Brown, R. S. Craxton, R. L. Keck, J. P. Knauer, J. H. Kelly, T. J. Kessler, S. A. Kumpan, S. J. Loucks, S. A. Letzring, F. J. Marshall, R. L. McCrory, S. F. B. Morse, W. Seka, J. M. Soares, and C. P. Verdon, *Opt. Commun.* **133**, 495 (1997).

7. S. Skupsky, R. W. Short, T. Kessler, R. S. Craxton, S. Letzring, and J. M. Soures, *J. Appl. Phys.* **66**, 3456 (1989).
8. *LLE Review Quarterly Report* **78**, 62, Laboratory for Laser Energetics, University of Rochester, Rochester, NY, LLE Document No. DOE/SF/19460-295 (1999).
9. S. P. Regan, J. A. Marozas, R. S. Craxton, J. H. Kelly, W. R. Donaldson, P. A. Jaanimagi, D. Jacobs-Perkins, R. L. Keck, T. J. Kessler, D. D. Meyerhofer, T. C. Sangster, W. Seka, V. A. Smalyuk, S. Skupsky, and J. D. Zuegel, *J. Opt. Soc. Am. B* **22**, 998 (2005); S. P. Regan, J. A. Marozas, J. H. Kelly, T. R. Boehly, W. R. Donaldson, P. A. Jaanimagi, R. L. Keck, T. J. Kessler, D. D. Meyerhofer, W. Seka, S. Skupsky, and V. A. Smalyuk, *J. Opt. Soc. Am. B* **17**, 1483 (2000).
10. S. Skupsky and R. S. Craxton, *Phys. Plasmas* **6**, 2157 (1999).
11. J. E. Rothenberg, *J. Opt. Soc. Am. B* **14**, 1664 (1997).
12. P. B. Radha, V. N. Goncharov, T. J. B. Collins, J. A. Delettrez, Y. Elbaz, V. Yu. Glebov, R. L. Keck, D. E. Keller, J. P. Knauer, J. A. Marozas, F. J. Marshall, P. W. McKenty, D. D. Meyerhofer, S. P. Regan, T. C. Sangster, D. Shvarts, S. Skupsky, Y. Srebro, R. P. J. Town, and C. Stoeckl, *Phys. Plasmas* **12**, 032702 (2005).
13. J. A. Marozas, S. P. Regan, J. H. Kelly, D. D. Meyerhofer, W. Seka, and S. Skupsky, *J. Opt. Soc. Am. B* **19**, 7 (2002).
14. *LLE Review Quarterly Report* **85**, 39, Laboratory for Laser Energetics, University of Rochester, Rochester, NY, LLE Document No. DOE/SF/19460-378, NTIS Order No. PB2006-106656 (2000).
15. P. W. McKenty, J. A. Marozas, V. N. Goncharov, K. S. Anderson, R. Betti, D. D. Meyerhofer, P. B. Radha, T. C. Sangster, S. Skupsky, and R. L. McCrory, *Bull. Am. Phys. Soc.* **51**, 295 (2006).
16. J. W. Goodman, *Introduction to Fourier Optics* (McGraw-Hill, New York, 1988).
17. J. W. Goodman, *Statistical Optics*, Wiley Series in Pure and Applied Optics (Wiley, New York, 1985).
18. J. A. Marozas and P. B. Radha, *Bull. Am. Phys. Soc.* **47**, 99 (2002).